

Unsupervised deep learning model for correcting Nyquist ghosts of single-shot spatiotemporal encoding

Qingjia Bao¹ | Xinjie Liu^{1,2} | Jingyun Xu³ | Liyang Xia³ | Martins Otikovs⁴ | Han Xie¹ | Kewen Liu³ | Zhi Zhang¹ | Xin Zhou^{1,2,5} | Chaoyang Liu^{1,2,5}

¹Key Laboratory of Magnetic Resonance in Biological Systems, Innovation Academy for Precision Measurement Science and Technology, Wuhan, China

²University of Chinese Academy of Sciences, Beijing, China

³School of Information Engineering, Wuhan University of Technology, Wuhan, China

⁴Weizmann Institute of Science, Rehovot, Israel

⁵Optics Valley Laboratory, Wuhan, China

Correspondence

Chaoyang Liu, Key Laboratory of Magnetic Resonance in Biological Systems, Innovation Academy for Precision Measurement Science and Technology, Wuhan, China
Email: chyliu@apm.ac.cn

Funding information

Chinese Academy of Sciences, Grant/Award Number: YZ201677; National Major Scientific Research Equipment Development Project of China, Grant/Award Number: 81627901; National Natural Science Foundation of China, Grant/Award Numbers: 11575287, 11705274; National key of R&D Program of China, Grant/Award Numbers: 2016YFC1304702, 2018YFC0115000, 2022YFF0707001, 2023YFE0113300

Abstract

Purpose: To design an unsupervised deep learning (DL) model for correcting Nyquist ghosts of single-shot spatiotemporal encoding (SPEN) and evaluate the model for real MRI applications.

Methods: The proposed method consists of three main components: (1) an unsupervised network that combines Residual Encoder and Restricted Subspace Mapping (RERSM-net) and is trained to generate a phase-difference map based on the even and odd SPEN images; (2) a spin physical forward model to obtain the corrected image with the learned phase difference map; and (3) cycle-consistency loss that is explored for training the RERSM-net.

Results: The proposed RERSM-net could effectively generate smooth phase difference maps and correct Nyquist ghosts of single-shot SPEN. Both simulation and real in vivo MRI experiments demonstrated that our method outperforms the state-of-the-art SPEN Nyquist ghost correction method. Furthermore, the ablation experiments of generating phase-difference maps show the advantages of the proposed unsupervised model.

Conclusion: The proposed method can effectively correct Nyquist ghosts for the single-shot SPEN sequence.

KEYWORDS

deep learning, Nyquist ghosts, single shot scan, spatiotemporal encoding, unsupervised

Qingjia Bao and Xinjie Liu contributed equally to this work.

1 | INTRODUCTION

Single-shot MRI can shorten the scanning time of multiscan MRI from several minutes to tens of milliseconds and has played an important role in functional MRI,¹ DTI,² dynamic contrast-enhanced perfusion imaging,³ and cardiac imaging.⁴ EPI⁵ is one of the most commonly used single-shot imaging methods; however, the inherent low phase-encoding (PE) bandwidth (<200 Hz clinical, <2000 Hz preclinical) of EPI often leads to serious artifacts.^{6,7} Single-shot spatiotemporal encoding (SPEN) introduces a linear swept-frequency chirp pulse in the PE dimension, which can effectively improve the bandwidth of the PE dimension and overcome susceptibility artifacts.^{8,9} Another advantage of the SPEN sequence is that it can directly obtain low-resolution images by performing Fourier transform (FT) along the readout (RO) direction. Thus, in SPEN aliasing, artifacts are absent when its signals are undersampled along the low-bandwidth dimension. This advantage is explored in many studies for interleaved high-resolution diffusion MRI with referenceless scans.^{10,11}

Like EPI, SPEN uses an alternate polarity gradient to reduce the acquisition time. Due to hardware imperfections¹² and eddy currents,¹³ phase shift always occurs between the k-space lines collected using the opposite gradient polarity, resulting in Nyquist ghosts in EPI images or superresolution (SR)¹⁴ SPEN images. There has increased the research on correcting Nyquist ghosting,^{15–19} and one of the most commonly used methods is the navigator-based method, which uses k-space lines without PE gradients to calculate the phase difference between even and odd images. However, due to the complex nonuniformity of the field, the linear assumption of phase change is not accurate enough, especially in high-field MR acquisition. As we mentioned previously, one advantage of the SPEN sequence is that it can directly obtain low-resolution images and do the Nyquist ghost correction without the need for reference scans^{17–19} or parallel-imaging techniques.⁴ Previous reports by Seginer et al.²⁰ and Chen et al.²¹ show that two low-resolution SPEN images obtained respectively from even echo data and odd echo data of a single SPEN data can provide information on phase inconsistency for implementing 2D Nyquist ghost correction without reference scans. However, it is still difficult for conventional methods to correct the Nyquist ghosts in SPEN images perfectly because of the phase-wrap problem, especially for low SNR images.

Recently, more and more researchers have applied deep learning methods in the field of MRI Nyquist ghost correction as the strong feature extraction ability of convolutional neural networks.^{22–24} Lee et al.²² combined deep learning with a low-rank Hankel matrix based on an

annihilating filter to correct Nyquist ghosts in EPI images; this represented the phase-mismatch correction problem as a missing k-space line interpolation problem for even and odd k-space data. Chen et al.²³ proposed an end-to-end Nyquist ghost-correction model based on U-net²⁵ for the EPI sequence. This method corrected Nyquist ghosts in the image domain, but the corrected amplitude image is prone to blurring. Wang et al.²⁴ corrected Nyquist ghosts by using a complex-valued network to reconstruct multicoil images without requiring coil sensitivity maps. However, all these deep learning-based Nyquist ghost-correction methods are supervised, which requires paired data sets during network training. In real MRI experiments, it is usually challenging to obtain such paired data sets. In addition, supervised methods are susceptible to distribution shifts and often yield unsatisfactory results on examples that do not pertain to the distribution of the training data.^{26,27}

In this paper, we propose a new unsupervised Nyquist ghost-correction method that takes advantage of spatiotemporal encoding, which provides PE information directly in the spatial domain and a deep learning model that can solve complex problems. The deep learning model works in an unsupervised way that does not need paired data sets to train (RERSM-net), and it can be applied to data from different domains without the need for additional training. First, we use the residual encoder (RE)²⁸ to extract the phase-difference map based on the even and odd images. As the SPEN pulse sequence provides direct spatial information in the PE dimension and can avoid the folding problem, it is relatively easy to obtain the phase information from the even and odd images. Then, the phase-difference maps between the even and odd images are generated by the restricted subspace mapping (RSM).^{29–31} Third, the physical model of SPEN is applied to obtain the SR cycle-back images. Finally, the network is trained by exploring the cycle-consistency loss between the corrected images and SR cycle-back images. Both simulation and real in vivo MRI experiments demonstrated that our method could correct the Nyquist ghosts in the SPEN experiment.

2 | METHODS

2.1 | Theory of Nyquist ghosts in single-shot SPEN

To make this paper self-contained, we briefly review the SPEN sequence and Nyquist ghost correction in SPEN. A fully refocused single-shot SPEN sequence enabling multislicing¹⁰ is used in this study and is shown in Figure 1A. The pulse sequence starts with a conventional slice selection, after which a delay equal to half of the total

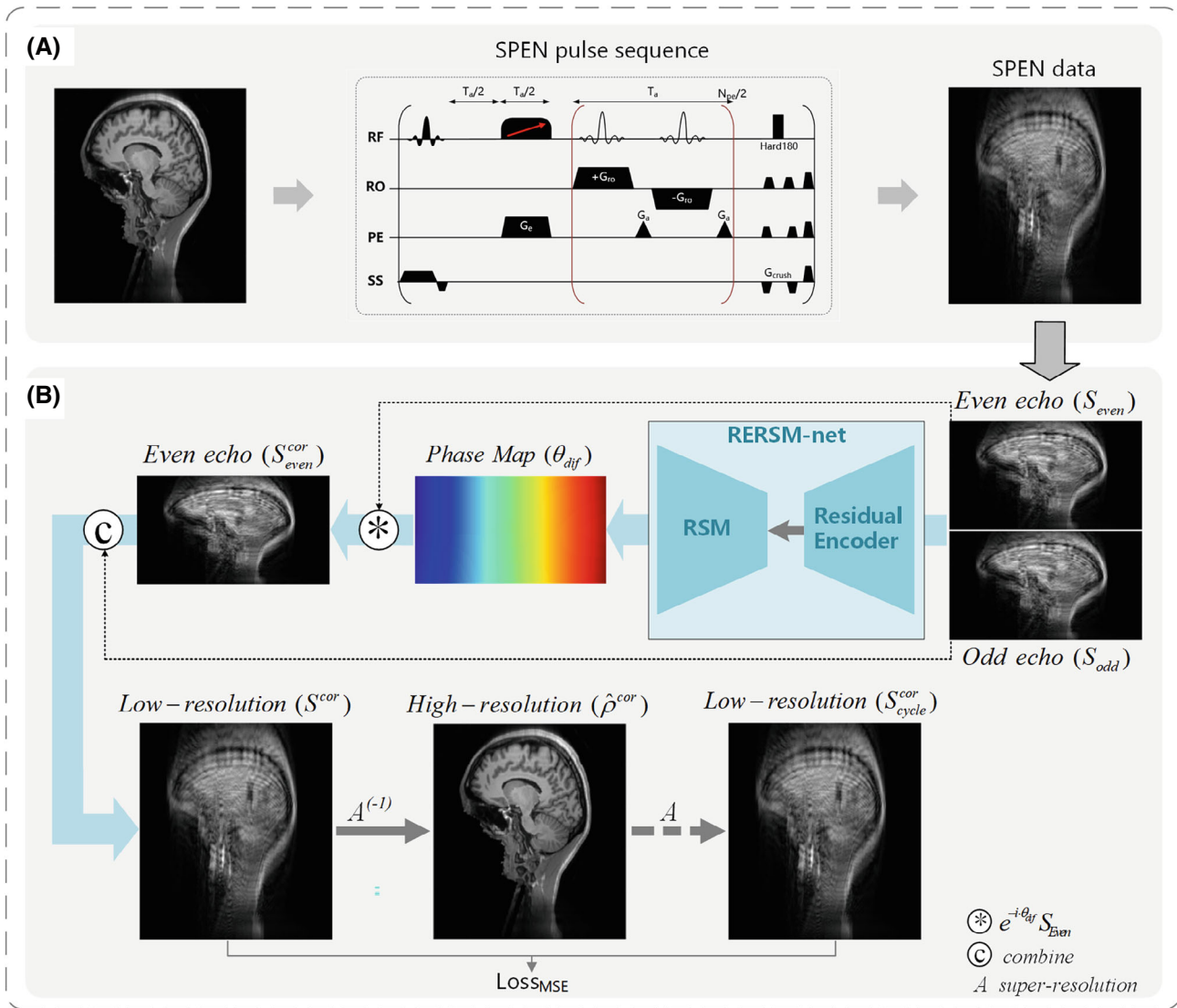


FIGURE 1 Overall architecture of the proposed unsupervised model for correcting Nyquist ghosts of single-shot spatiotemporal encoding (SPEN), with the real and imaginary components of the low-resolution odd echo image S_{odd} and even echo image S_{even} as input, and a complex high-resolution ghost-corrected image $\hat{\rho}^{cor}$ as output. The residual encoder and restricted subspace mapping network (RERSM-net) includes a residual encoder module and a restricted subspace mapping (RSM) module. The mean-squared error (MSE) loss between the low-resolution, phase-corrected SPEN image S^{cor} and superresolution cycle-back image S_{cycle}^{cor} is explored to train the network.

acquisition time is inserted, followed by an application of a linear frequency-swept chirp pulse in conjunction with a gradient along the PE direction of a duration equal to half the total acquisition time. This choice of chirp duration together with the previous delay ensures T_2^* refocusing of each acquired RO echo in contrast to EPI, where only echo at the center of k-space is T_2^* refocused. Application of a linear frequency sweep in the presence of a gradient results in a spatially dependent quadratic phase profile, and the decoding gradient blips G_a along the PE direction are used to sequentially refocus the spins along the PE dimension and displace the apex of the quadratic phase profile in order to traverse the whole FOV along the PE dimension.⁸ After performing FT along the RO direction,

the SPEN signal of the k-space points k_m can be described as follows:

$$S(k_m) \propto \int \rho(y) e^{i(ay^2 + by + k_m y)} dy \quad (1)$$

where y represents the coordinate of PE dimension; $\rho(y)$ represents the spin density; a and b represent the quadratic and linear phase coefficients, respectively. Equation (1) indicates that the SPEN image can be extracted by the stationary phase approximation through $\rho(y) \propto |S(k_m(y))|$ with resolution limited to $\sqrt{\pi/|a|}$.³² To improve the resolution, the SR¹⁴ method is always needed, in which the phase integral in Equation (1) assumes a discretized object made of N elements:

$$S(k_m) \approx \sum_{n=1}^N \hat{\rho}_n \int e^{i(ay^2+by+k_my)} dy = \sum_{n=1}^N \hat{\rho}_n A_{mn} \quad (2)$$

where $\hat{\rho}_n$ represents the approximate density in voxel n , and A_{mn} represents an element of the SR matrix A . Equation (2) can be rewritten in matrix form as $S = A\hat{\rho}$, and the imaged object $\hat{\rho}$ can thus be determined by applying the inverse matrix of A , $A^{(-1)}$ onto S , $\hat{\rho} = A^{(-1)}S$.³²

In single-shot experiments, the rapid change of the RO gradients will cause a phase mismatch θ_{dif} between even echo signal S_{even} and odd echo signal S_{odd} , as follows:

$$\frac{S_{\text{odd}}}{S_{\text{even}}} = e^{i\theta_{\text{dif}}} \quad (3)$$

Affected by the characteristics of the SR matrix A , the even/odd phase difference can easily result in Nyquist ghosts in the high-resolution SR image $\hat{\rho}$ of S .²⁰ Conventional methods^{20,21} usually eliminate the Nyquist ghosts by estimating the phase difference θ_{dif} and correcting it (the details can be found in Figure S1):

$$\left\{ \begin{array}{l} S_{\text{even}}^{\text{cor}} = e^{-i\theta_{\text{dif}}} S_{\text{even}} \\ S^{\text{cor}} = \begin{bmatrix} \begin{pmatrix} S_{\text{odd}}(1, 1) \\ S_{\text{even}}^{\text{cor}}(1, 1) \\ S_{\text{odd}}(2, 1) \\ S_{\text{even}}^{\text{cor}}(2, 1) \\ \vdots \end{pmatrix} & \cdots & \begin{pmatrix} S_{\text{odd}}(1, Q) \\ S_{\text{even}}^{\text{cor}}(1, Q) \\ S_{\text{odd}}(2, Q) \\ S_{\text{even}}^{\text{cor}}(2, Q) \\ \vdots \end{pmatrix} \\ \hat{\rho}^{\text{cor}} = A^{(-1)} S^{\text{cor}} \end{array} \right. \quad (4)$$

where $S_{\text{even}}^{\text{cor}}$ represents the phase-corrected even echo signal; S^{cor} represents the fully phase-corrected signal; $A^{(-1)}$ represents the operation used for SR; and $\hat{\rho}^{\text{cor}}$ represents the high-resolution ghost-corrected image.

2.2 | Model for Nyquist ghost correction

This work aims to design an unsupervised Nyquist ghost-correction model based on a RERSM-net. The overall architecture of this new model is shown in Figure 1B, which primarily includes three steps: First, we take the four-channel images (the real part image and imaginary part image of low-resolution even and odd images) as the input of the RERSM-net to extract the phase information, and generate the phase-difference map between the low-resolution even and odd images; then, we use the phase-difference map to correct the phase of the low-resolution even image; and finally, we recombine the low-resolution, phase-corrected even image with the low-resolution odd image to obtain a full low-resolution,

phase-corrected image and apply SR reconstruction to obtain the final high-resolution, ghost-corrected image.

The detailed structure of RERSM-net is shown in Figure 2. It contains a RE module (Figure 2A) and a RSM module (Figure 2B). The main idea of the RE module is to generate the coefficients for the phase-difference map in the restricted subspace of the RSM module (i.e., these coefficients are expected to be close to the inner product of the phase-difference map and the predefined cubic spline vectors in RSM).^{29–31} Cubic spline basis function is a commonly used mathematical function in interpolation and fitting problems. They are used for smooth interpolation or fitting of curves between discrete data points. Cubic spline basis functions consist of multiple cubic polynomials, which are called basis functions, and smoothly connect adjacent data points. By reasonably selecting cubic spline basis functions, using cubic splines for interpolation or fitting, and calculating the inner product between the basis function vectors to determine the weight or coefficient of the interpolation or fitting curve, the data interpolation and fitting can be effectively carried out, thereby obtaining curves that meet the requirements of data features and smoothness. The RE module consists primarily of multiple residual blocks³³ and down-sampling operation. The residual block is combined with the down-sampling to extract the deep phase feature of the input low-resolution even and odd images gradually. The residual connection is introduced in each residual block to prevent the network from overfitting. At the output end of the RE module, a 1×1 convolution layer is performed to fuse the multichannel feature maps, yielding a single-channel phase feature map. At the same time, the Leaky ReLU (rectifier linear unit) is used after the 1×1 convolution layer to convert the phase feature map to the coefficients and ensure that the value of the coefficients can be positive or negative. Two sets of predefined cubic spline vectors (basic matrices) (i.e., calculating the inner product of the basic matrices and the deep-learned coefficients matrix) form the RSM module. These two matrices form the inner product to obtain the corresponding predicted phase-difference map in the image space.

2.3 | Unsupervised loss function

In this study, we introduce a new, unsupervised, cycle-consistency loss function between the corrected images and SR cycle-back images. This loss function relies on the fact that the inverse of A does not necessarily exist due to the large condition number of A ; consequently, $A^{(-1)}A$ is not equal to the identity, producing images with ghosts, if no additional measures are taken to reduce the condition number of A .^{20,21} As a result, this implies

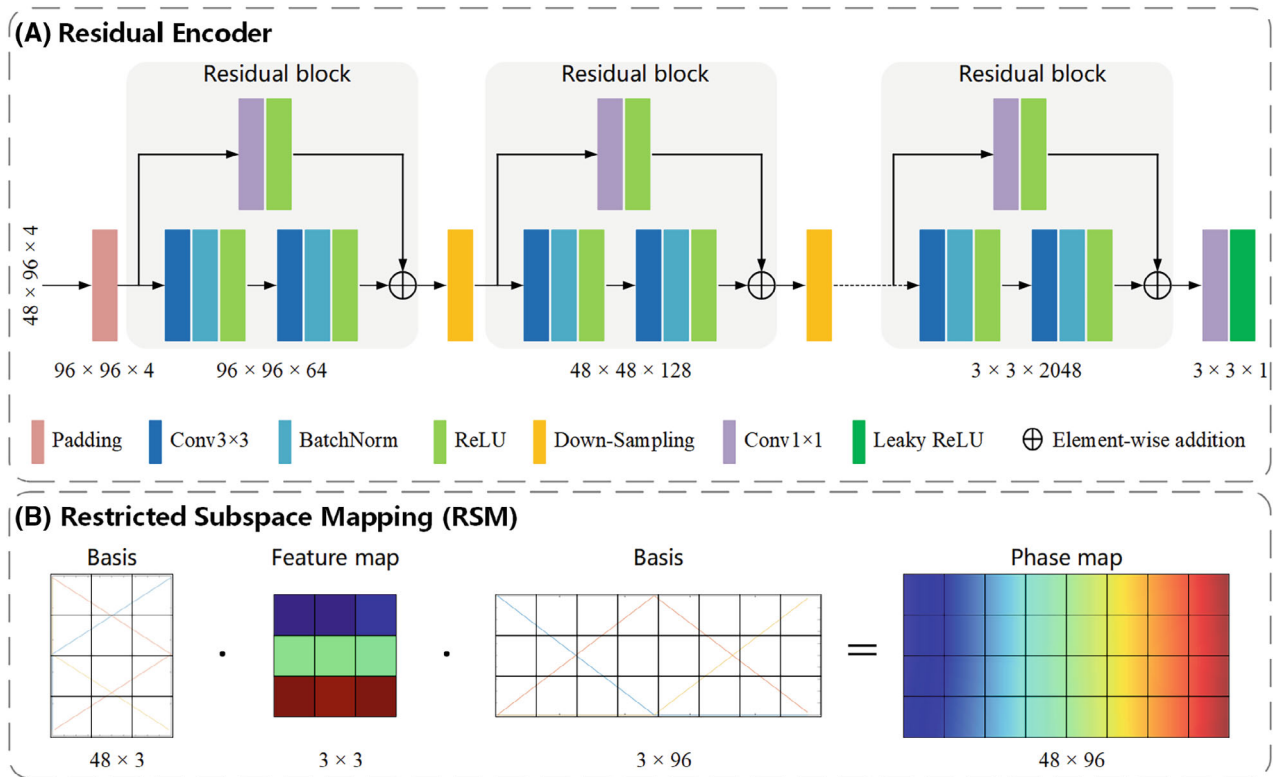


FIGURE 2 (A) Detailed structure of the residual encoder module, including multiple cascaded blocks. Combine the residual block with the down-sampling operation to gradually extract the deep phase feature and introduce the residual connection into each residual block to avoid network overfitting. Use a 1×1 convolution layer to fuse the multichannel feature maps to generate a single-channel phase feature map and use a Leaky ReLU (rectifier linear unit) to ensure that the phase value can be positive or negative. (B) Principle of the restricted subspace mapping module. Mapping the deep phase feature (size = 3×3) extracted by the residual encoder to a smooth phase-difference map (size = 48×96) through two sets of predefined basis matrices (size = 48×3 and 3×96).

that, due to deviation of $A^{(-1)}A$ from identity, increased phase difference between the even and odd echoes will lead to higher error between the corrected image and image obtained after applying $A^{(-1)}A$ to the corrected image. This is illustrated in Figure 3C, where the bigger the phase difference between even and odd images, the larger the cycle-consistency loss will be. In Figure 3, S represents the low-resolution SPEN image; $\hat{\rho}$ represents the high-resolution SR image of S ; S_{cycle} represents the low-resolution SR cycle-back image of S ; and Loss represents the mean-squared error (MSE) between S and S_{cycle} . It can be described as follows:

$$\begin{cases} \hat{\rho} = A^{(-1)}S \\ S_{\text{cycle}} = A\hat{\rho} \\ \text{Loss} = \text{MSE}(S, S_{\text{cycle}}) \end{cases} \quad (5)$$

Taking the linear even/odd phase difference ($ax + b$, where a is the linear coefficient and b is the constant) as an example, the larger the a and b , the more severe the Nyquist ghosts in SR image $\hat{\rho}$ and the larger the Loss between low-resolution SPEN image S and SR cycle-back

image S_{cycle} . Based on this SR cycle-consistency characteristic of SPEN, we propose an unsupervised loss function that does not need the ground-truth image, but only calculates the MSE loss between the full low-resolution, phase-corrected SPEN image S^{cor} and SR cycle-back image $S_{\text{cycle}}^{\text{cor}}$ (Figure 1B). The proposed unsupervised cycle-consistency loss function is described as follows:

$$\text{Loss}_{\text{MSE}} = \frac{1}{w \times h} \sum_{i=1}^w \sum_{j=1}^h (S^{\text{cor}}(i, j) - S_{\text{cycle}}^{\text{cor}}(i, j))^2 \quad (6)$$

where w and h represent the width and height of S^{cor} , respectively; $S^{\text{cor}}(i, j)$ represents the pixel value at position (i, j) of S^{cor} ; and $S_{\text{cycle}}^{\text{cor}}(i, j)$ represents the pixel value at position (i, j) of $S_{\text{cycle}}^{\text{cor}}$.

2.4 | Comparison between supervised training and unsupervised training

As we all know, supervised methods face some limitations that can be addressed by unsupervised approaches.

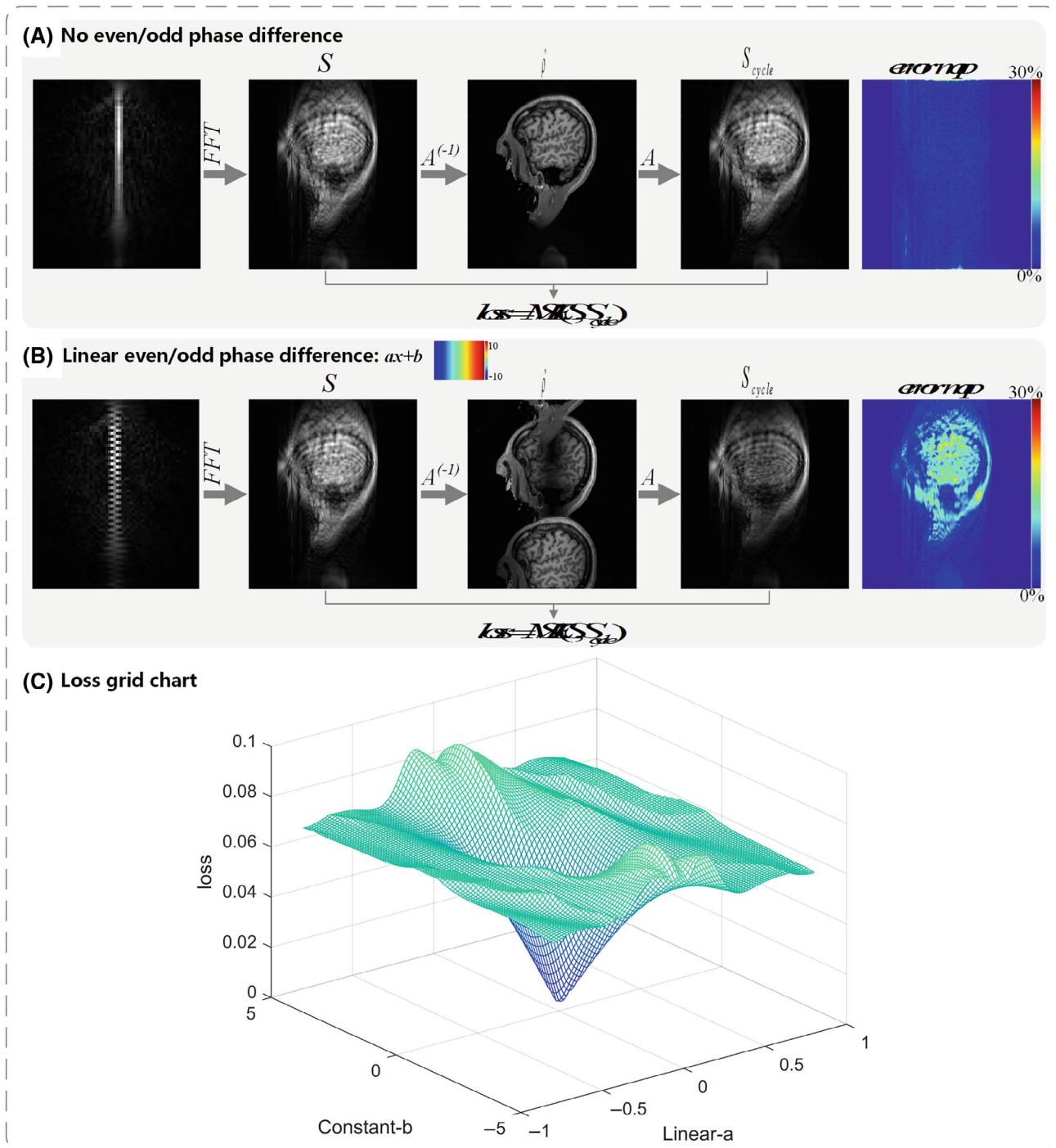


FIGURE 3 Cycle-consistency loss between the Nyquist ghost-corrected images and superresolution (SR) cycle-back images to train the network. S represents the low-resolution spatiotemporal encoding (SPEN) image; \hat{p} represents the high-resolution SR image; and S_{cycle} represents the low-resolution cycle-back image of S . (A) No phase difference between the even and odd echoes of S . (B) Linear phase difference ($ax + b$) between the even and odd echoes of S . (C) Grid chart of the unsupervised loss; the x-axis represents the linear coefficient a ($-1 \sim 1$), and the y-axis represents the constant b ($-5 \sim 5$). The smaller the a and b , the smaller the loss between S and S_{cycle} . FFT, fast Fourier transform.

First, a large amount of data with ground truth is routinely required for network training when supervised methods are used. Second, unsupervised networks are more immune to distribution shifts and display much higher robustness toward out-of-distribution samples.^{26,27}

To demonstrate this advantage, the comparison between supervised training and unsupervised training was also examined. All models are trained on human data and are tested either on the simulated human or rat data. As we can observe from Figure S2, three kinds of training

are performed in this work. The first one is the supervised end-to-end training, and the input of the model is high-resolution uncorrected images (after the SR of the low-resolution images with even/odd phase difference). The training loss is set to the MSE between the output of the network and the ground-truth images that are obtained by the simulation with no even/odd phase error. Here, the model Dense-net³⁴ was used. The second kind of training is also supervised; however, we introduce the physical model here. The even/odd problem can be addressed by applying the phase-difference map that originates from the alternate polarity gradients. Thus, the network is trained to obtain the phase-difference map rather than the final images, and the training loss is also set to the MSE between the output of the network and the ground-truth images. The model is Dense-net or RERSM-net. The last kind is the unsupervised model that is used in this work. The training loss is the cycle-consistency loss between the corrected images and SR cycle-back images.

2.5 | Experiments

To quantitatively compare the Nyquist ghost-correction results, single-shot SPEN simulations were performed based on the T₁-weighted (T₁w) images downloaded from the Human Connectome Project website.^{35,36} All the T₁w images were acquired on the standard Human Connectome Project 3T Siemens MRI scanner with 32-channel head coil. To obtain SPEN images, the pulse sequence depicted in Figure 1A was simulated with the corresponding acquisition and encoding parameters: FOV = 4 × 4 cm², sampling matrix = 256 × 256 (RO × PE), effective TE = 36.0 ms, TR = 4.0 s, R-value of chirp pulse = 400, and pulse length = 18 ms. A total of 32 spins per voxel were used to avoid discontinuities, and the simulations were performed in *MATLAB* using the Spintool package (Tal 2020; Visual Display Interface [VDI] computer software; retrieved from <http://www.vdisoftware.net>). The details of the simulations can be found in Figure S3. A total of 3000 simulated slices (size = 256 × 256) were obtained: 1800 slices for training, 200 slices for validation, and 1000 slices for testing. The slices from different subjects were pooled together and randomly divided in training, validation, and testing sets without considering to which subject each slice pertained. Due to data splitting in a non-subject-specific manner, there could be a possibility that similar slices from the same subject are included in different data sets and cause the potential bias for the network. However, we do not expect this to affect the overall results, as the network is trained in an unsupervised manner, relying on a physical model-based cost function with cycle consistency loss. It

is also worth noting that the network presented herein will only perform the phase correction between even and odd data; hence, it will not change the energy of the images. Therefore, although we do the correction for every single slice, the intensity of the whole subject will remain constant.

The real MRI data were acquired on a Bruker Biospec 7T/20-cm MRI scanner using a RARE³⁷ sequence, single-shot EPI sequence, and single-shot SPEN sequence of water phantom, orange, cucumber, and in vivo rats. The specific sequence parameters can be found in Table S1. For all the water phantom, orange, and cucumber experiments, a 72-mm-diameter volume coil was used for both RF transmission and signal detection. For the in vivo rat experiment, a 72-mm-diameter volume coil was used for RF transmission and a quadrature surface coil for signal detection. The rats were anesthetized with isoflurane mixed with oxygen (4.0%–5.0% for induction, 0.5%–1.0% for maintenance). The respiratory rate (~30–50) was continuously monitored during the scan under the anesthesia. The body temperature was maintained with 37°C water circulation. All animal experiments were conducted following the National Institutes of Health animal care guidelines, and the procedures were approved by the Animal Ethics Committee of Innovation Academy for Precision Measurement Science and Technology, Chinese Academy of Sciences (APM22022A).

In this study, the conventional method,²⁰ the state-of-the-art supervised Dense-net method,³⁴ and U-net were used for the comparison with RERSM-net. As mentioned in Section 2.4, the Dense-net was used for comparing supervised and unsupervised learning, and U-net was used for comparing the proposed RERSM-net. In terms of the model parameters, Dense-net has 1.48 million, RERSM-net has 19.58 million, and U-net has 34.53 million parameters. More information on U-net can be found in Figure S4 and Table S2. The objective evaluation for simulated data adopts the commonly used peak SNR (PSNR), structural similarity index measurement (SSIM),³⁸ and correction time for one slice. All the deep learning-based experiments were performed in the PyTorch framework for the *Python* 3.7 environment, and the training strategies were optimized in the same computer system with Intel i7-8700 K CPU, 32 GB RAM, and an NVIDIA Geforce GTX 2080 Ti with 11 GB GPU memory. In terms of training parameters, an Adam optimizer³⁹ was used to train the network and update the network parameters. The initial learning rate was set to 0.0005, and it decayed by a factor of 0.95 after 5 epochs. The batch size was 4, and a total of 150 epochs were trained (the source code is available at https://github.com/baoqingjia/SPEN_correction).

3 | RESULTS

3.1 | Validation for simulated data

Figure 4A shows the Nyquist ghost-correction results for one representative slice of simulated data with a linear phase difference map. Figure 5A shows the Nyquist ghost-correction results for one representative slice of simulated data with a nonlinear phase difference map. For each slice, the first row shows the uncorrected ghost image, ground-truth image, and ghost-corrected images of the conventional method, state-of-the-art supervised deep learning method (Dense-net³⁴), and the proposed unsupervised RERSM-net. The second row shows the

zoomed region of the first row's images, and the third row shows the reference phase-difference map in the simulation experiment and corresponding phase-difference maps obtained by the conventional method, Dense-net, and the proposed RERSM-net. Figures 4A and 5A illustrate that RERSM-net can obtain much better ghost-corrected images compared with the conventional method. This can be particularly well perceived from the zoomed images shown in the second row. There are remaining Nyquist ghosts in the images corrected by the conventional method, especially in the case of a nonlinear phase difference map. However, regardless of linear or nonlinear phase difference map, the proposed RERSM-net can correct Nyquist ghosts effectively.

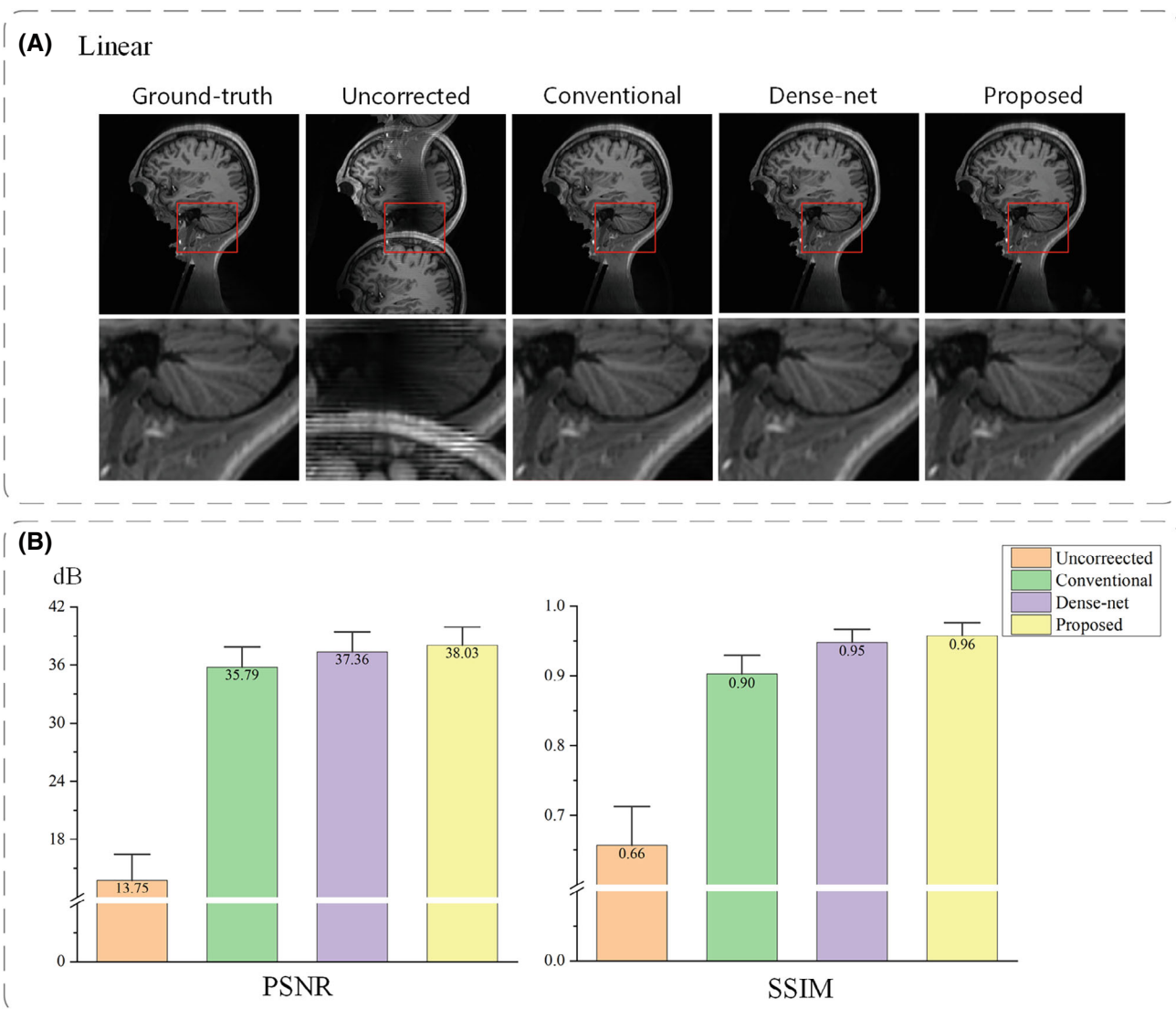


FIGURE 4 Nyquist ghost-correction results for one representative slice of simulated data with a linear phase-difference map. (A) The first row from left to right shows the ground-truth image, uncorrected ghost image, and ghost-corrected images of the conventional method and proposed residual encoder and restricted subspace mapping network, respectively. The second row shows the zoomed region of the first row's images. (B) Quantitative results of peak SNR (PSNR) and structural similarity index measurement (SSIM) for various comparison methods.

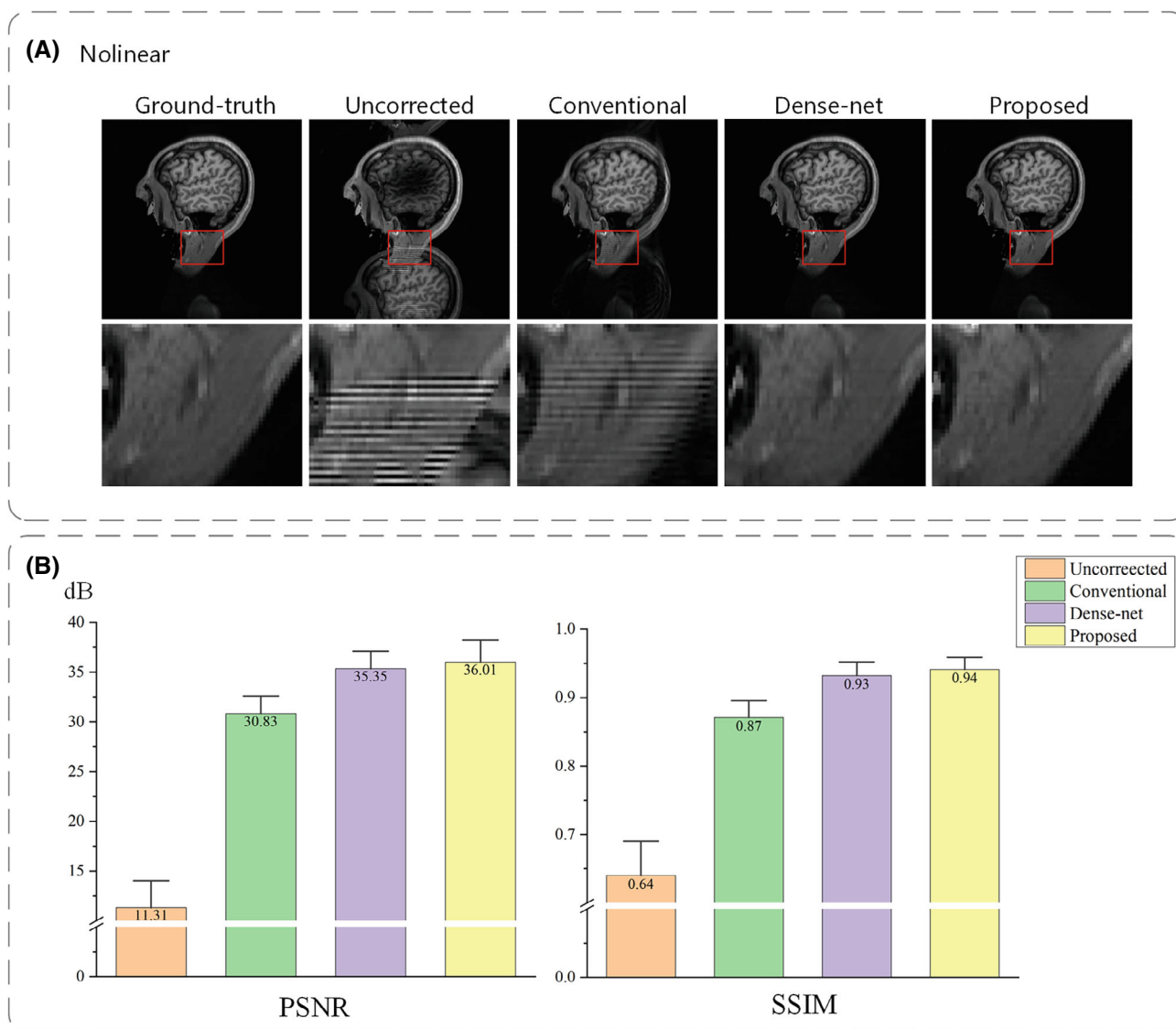


FIGURE 5 Nyquist ghost-correction results for one representative slice of simulated data with a nonlinear phase difference map. (A) The first row from left to right shows the ground-truth image, uncorrected ghost image, and ghost-corrected images of the conventional method and proposed residual encoder and restricted subspace mapping network, respectively. The second row shows the zoomed region of the first row's images. (B) Quantitative results of peak SNR (PSNR) and structural similarity index measurement (SSIM) for various comparison methods.

Similarly, Dense-net also performs much better than the conventional ghost-correction method.

Figure 4B summarizes the quantitative comparison between the uncorrected ghost images and the ghost-corrected images of the conventional method, Dense-net, and the proposed RERSM-net on the whole simulated test-data linear phase-difference map. In terms of PSNR/SSIM quantitative metrics, the proposed RERSM-net score is 38.03 ± 2.08 dB/ 0.96 ± 0.02 , which is higher compared with 35.79 ± 2.59 dB/ 0.90 ± 0.03 for the conventional method, 37.36 ± 2.93 dB/ 0.95 ± 0.04 for Dense-net, and 13.75 ± 4.12 dB/ 0.66 ± 0.06 for the uncorrected ghost images. In terms of the Nyquist

ghost-correction time for a single slice, the conventional method takes 2.727 s with CPU, and the proposed RERSM-net takes only 9 ms with GPU, which is still less than 11 ms necessary for Dense-net. For nonlinear phase-difference correction, the proposed deep learning-based correction method can obtain much better results compared with the conventional method, as shown in Figure 5B. In terms of PSNR/SSIM quantitative metrics, the proposed RERSM-net score is 36.01 ± 2.42 dB/ 0.94 ± 0.03 , which is higher compared with 30.83 ± 3.16 dB/ 0.87 ± 0.05 for the conventional method, 35.35 ± 3.53 dB/ 0.93 ± 0.05 for Dense-net, and 11.31 ± 4.23 dB/ 0.64 ± 0.08 for uncorrected ghost images.

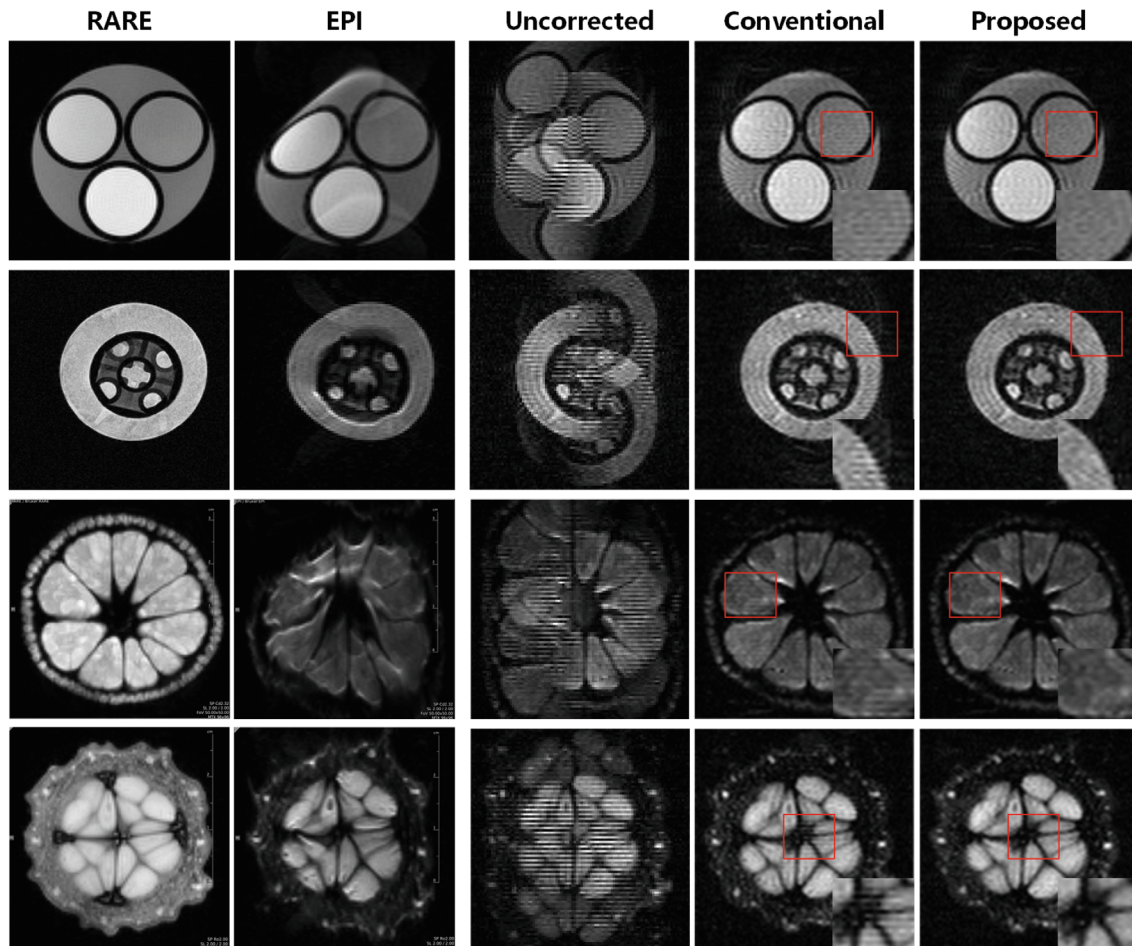


FIGURE 6 Nyquist ghost-correction results for water phantom, orange, and cucumber. The first and second rows show the results of water phantom, and the third and fourth rows show the results of orange and cucumber, respectively. The columns from left to right show the MR images obtained by the RARE sequence and single-shot EPI sequence with reference scan correction, the ghost-uncorrected spatiotemporal encoding (SPEN) images, and the ghost-corrected SPEN images for the conventional method and proposed residual encoder and restricted subspace mapping network, respectively.

3.2 | Results for real MRI data

Figure 6 shows the Nyquist ghost-correction results for two water phantoms, orange, and cucumber. The first and second rows show the results of the water phantom, and the third and fourth rows show the results of orange and cucumber, respectively. Figure 7 shows the Nyquist ghost-correction results for two representative slices of in vivo rats. The first column shows the MRI images obtained by the RARE sequence. The RARE images have high resolution with a clear texture of details, but the RARE sequence requires about 40 s of acquisition time for a single slice. The second column shows the MRI images obtained by the single-shot EPI sequence with reference scan correction.⁴⁰ However, the EPI images are distorted due to the inhomogeneous magnetic fields, especially evident for water phantom and orange. The third column shows the uncorrected ghost images obtained by the single-shot

SPEN sequence. The overlapping Nyquist ghosts obscure most of the details of the tissue. The fourth and fifth columns show the ghost-corrected images of the conventional method and proposed RERSM-net, respectively. The Nyquist ghosts still can be noticed in the images from the conventional method, especially in the zoomed regions. The proposed RERSM-net can correct Nyquist ghosts more effectively.

3.3 | Ablation experiment of the unsupervised RERSM-net

To examine the improved robustness of the unsupervised network (RERSM-net) toward out-of-distribution samples, we compare the supervised and the unsupervised models. All the models are trained on human data and tested on either the simulated human or rat data. The

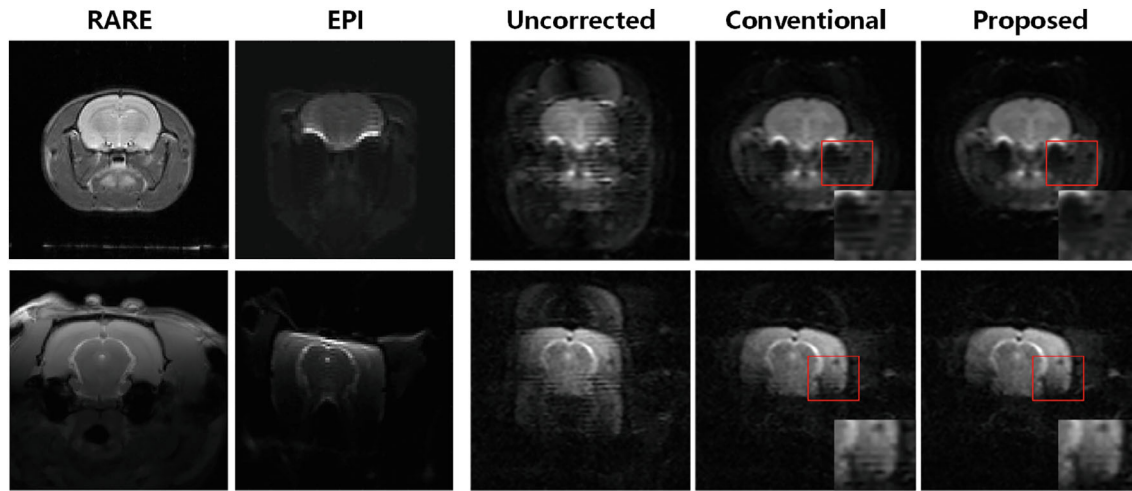


FIGURE 7 Nyquist ghost-correction results for two representative slices of in vivo rats. The columns from left to right show the MR images obtained by the RARE sequence and single-shot EPI sequence with reference scan correction, the ghost-uncorrected spatiotemporal encoding (SPEN) images, and the ghost-corrected SPEN images for the conventional method and proposed residual encoder and restricted subspace mapping network, respectively.

comparison results are shown in Figure 8. All three kinds of training can obtain good results for human data, as the model is training on human data. The PSNR/SSIM of unsupervised RERSM-net (38.03 ± 2.08 dB/ 0.96 ± 0.02) are almost similar to the metrics of the supervised Dense-net (37.36 ± 2.93 dB/ 0.95 ± 0.04), supervised RERSM-net (36.90 ± 2.23 dB/ 0.94 ± 0.04), and the conventional method (35.79 ± 2.59 dB/ 0.90 ± 0.03). However, the results delivered on rat data were significantly inferior for the supervised learning, even with the physical information of the SPEN. The PSNR/SSIM of unsupervised RERSM-net (30.01 ± 2.56 dB/ 0.90 ± 0.04) are much higher than the metrics of the supervised Dense-net (18.37 ± 4.32 dB/ 0.74 ± 0.08) and supervised RERSM-net (22.90 ± 3.55 dB/ 0.81 ± 0.06), and similar to the conventional method (34.06 ± 2.47 dB/ 0.92 ± 0.03). Conversely, the unsupervised model can still obtain good results for rat data when applying the pretrained, unsupervised model obtained by human data.

In addition, we replace RERSM-net with U-net and regard the output of U-net as the phase-difference map, training U-net with the same unsupervised loss as used for the RERSM-net training. The results are shown in Figure S5. It can be noticed that the phase-difference maps generated by U-net are still not sufficiently smooth and caused some Nyquist ghosts in the final, corrected images. The absolute error map of the conventional method is also larger, indicating that the corrected image of the proposed RERSM-net is closer to the ground-truth image. The PSNR/SSIM of RERSM-net is also much higher than the metrics of the U-net model. Additionally, an ablation experiment with or without residual block in the RERSM-net was also performed

(Figure S6) to demonstrate the advantage of the residual connection.

4 | DISCUSSION

This work has proposed a new method for Nyquist ghost correction in single-shot SPEN images that arise from the phase mismatch between even and odd echoes. As shown in Figures 4–7, both qualitative image and quantitative metrics demonstrate that our proposed method outperforms the state-of-the-art conventional method, especially in the case of a nonlinear phase-difference map. Additionally, the Nyquist ghost-correction time for a single slice in the proposed method is less than 10 ms, which is much shorter compared with the conventional method.

The main limitation of the conventional method may be due to phase unwrapping and quadratic polynomial fitting, especially for nonlinear phase-difference maps caused by eddy current, shown in Figure 5A. The conventional method uses the arctangent function to calculate the phase-difference map corresponding to the SR even and odd images, then applies phase unwrapping to restore the original phase value from the phase wrapped within a periodic interval ($-\pi \sim \pi$). Due to the low SNR, phase unwrapping may introduce an accumulation of a phase error. In this work, we try to address this phase unwrap problem by deriving phase-difference maps by the deep learning method. Particularly, in the RERSM-net, we chose spline functions as our basis set, as shown in Figure 2B, where the feature maps in RE's output layer correspond to the coefficients in the restricted low-resolution

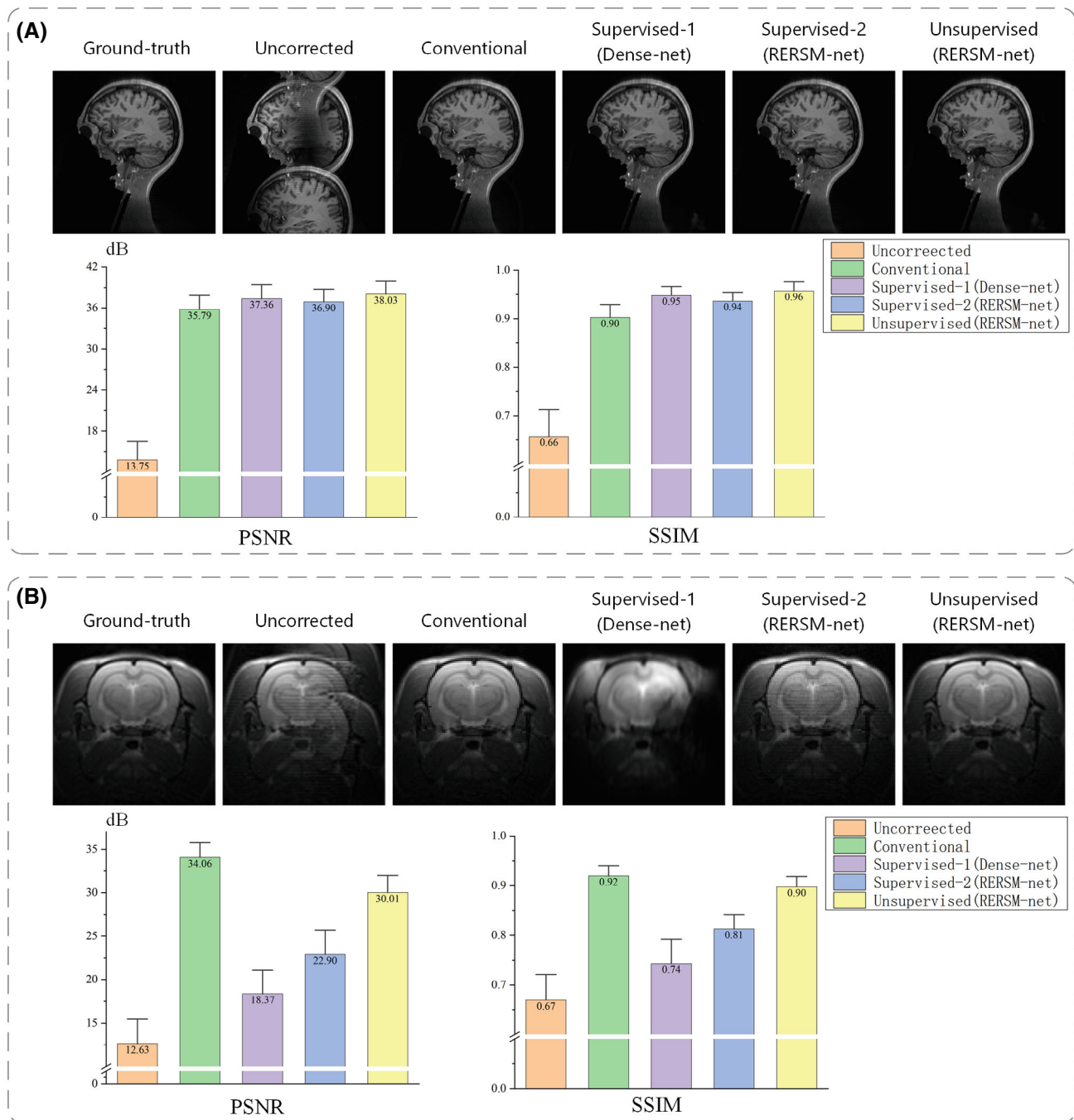


FIGURE 8 Reconstruction results of the unsupervised method and the supervised method on human data (A) and rat data (B). The first row from left to right shows the ground-truth image, uncorrected ghost image, and ghost-corrected images of the conventional method, supervised Dense-net, supervised residual encoder and restricted subspace mapping network (RERSM-net), and unsupervised RERSM-net, respectively. The second row shows the quantitative results of peak SNR (PSNR) and structural similarity index measurement (SSIM) for various comparison methods.

subspace. First, this helps to avoid discontinuities in the derived phase-difference maps, as using a set of smooth basis functions can enforce smoothness on the phase-difference map, by definition. However, for certain cases it might be necessary to extend the set of basis functions to include higher-order splines to account for rapidly changing phase in phase-difference maps, such as

in the presence of flow or severe variations in magnetic field susceptibility. Nonetheless, even in these cases, we expect the phase-difference map between even and odd echoes to be smooth in the sense of not having discontinuities. Second, use of spline functions reduces the number of parameters by constraining the phase-difference map to a subspace spanned by the basis functions. The

number of parameters is 19.58 million, which is almost half the number of parameters of a common U-net (34.49 million).

It is worth mentioning that the main advantage of this Nyquist ghost-correction method is that it is based on unsupervised training, without ground-truth data (label), which is often challenging to obtain.⁴¹ We calculate the cost function using the physical forward problem based on the characteristic of spatiotemporal encoding during traditional training without a need for ground-truth data. With this physical forward model, we also try to correct the images directly from a single slice (“no pre-training network”). Although the generalization will not constitute a challenge for this “no pre-training network,” it will take much longer time to correct the images (~10 s for one image). In this work, we pretrained the network with only simulated data and tested the network with both simulated and real in vivo MRI data.

This new unsupervised model is only trained for the correction of Nyquist ghosts in single-shot SPEN. For future work, we plan to expand this unsupervised method for motion artifact correction in multishot SPEN.¹⁰ Compared with single-shot SPEN, the artifacts of multishot SPEN are more complex. Not only the phase difference between the even and odd echoes of each shot will cause Nyquist ghosts, but also the involuntary movement of the mice or humans will introduce the phase difference between each shot and cause motion artifacts, especially in diffusion-weighted MRI. In addition, SR in SPEN reconstruction is also an interesting inverse problem.^{42,43} In particular, some novel unpaired learning algorithms have been published to overcome the lack of paired data in the real world for SR.^{44–46} In the present scope of this paper, we limited ourselves to addressing only the even-odd phase-correction issue. However, we believe that the deep learning methods that combine SR and phase correction for SPEN will provide better images. We also plan in our future work to study and try to resolve the issues associated with the SR part.

In addition, SR formulated as an inverse problem in SPEN reconstruction is also of particular interest.^{42,43} In this context, some novel unpaired learning algorithms have recently been published to overcome the lack of paired data in the real-world applications of SR.^{44–46} However, in the present scope of this paper, we limited ourselves to addressing only the issue of even-odd phase correction. We believe that the deep learning methods that combine SR and even-odd phase correction and SR for SPEN will provide better images. We also plan in our future work to address resolving the issues associated with SR part.

Although in the present study we did not rely on multiple receiver information, our method could be integrated

with multiple receivers (i.e., multicoil information could be used to reconstruct higher-resolution, artifact-free images from even and odd echoes of SPEN acquisition using the SUSPENSE approach⁴⁷ (SENSE implementation in case of SPEN), similar to the MUSE approach⁴⁸ in which images for each of the interleaved shots are reconstructed to obtain per-shot phase maps. This would allow the determination of a more precise phase-difference map, particularly in the case if SPEN data are being undersampled along the PE direction, as, for example, would be the case of multishot SPEN, if for each shot even and odd echoes are analyzed separately.

5 | CONCLUSIONS

This work proposes a Nyquist ghost-correction deep learning model that takes advantage of both spatiotemporal encoding, which provides PE information directly in the spatial domain, and the deep learning model, which can offer a powerful way to solve complex problems. By exploring the cycle-consistency loss between the Nyquist ghost-corrected images and SR cycle-back images, this model is trained without explicit knowledge of the ground-truth phase-difference map or ground-truth data. Results using simulated and preclinical data sets demonstrate that our method outperforms the conventional method, and the speed is an order of magnitude faster.

ACKNOWLEDGMENTS

We gratefully acknowledge the financial support by the National Major Scientific Research Equipment Development Project of China (81627901), the National key of R&D Program of China (2016YFC1304702; 2018YFC0115000; 2022YFF0707001; 2023YFE0113300), National Natural Science Foundation of China (11575287 and 11705274), and the Chinese Academy of Sciences (YZ201677). We also gratefully acknowledge Chongxin Bai, Weida Xie, and Piqiang Li for their advice on experimental design and their timely help in analyzing a large number of samples.

DATA AVAILABILITY STATEMENT

The source code for this study is available at https://github.com/baoqingjia/SPEN_correction.

ORCID

Qingjia Bao  <https://orcid.org/0000-0003-0940-2535>

Xin Zhou  <https://orcid.org/0000-0002-5580-7907>

REFERENCES

1. Feinberg DA, Yacoub E. The rapid development of high speed, resolution and precision in fMRI. *Neuroimage*. 2012;62:720-725.
2. Tournier JD, Mori S, Leemans A. Diffusion tensor imaging and beyond. *Magn Reson Med*. 2011;65:1532-1556.

3. Shiroishi MS, Castellazzi G, Boxerman JL. Principles of T2*-weighted dynamic susceptibility contrast MRI technique in brain tumor imaging. *J Magn Reson Imaging*. 2015;41:296-313.
4. Kim YC, Nielsen JF, Nayak KS. Automatic correction of echo-planar imaging (EPI) ghosting artifacts in real-time interactive cardiac MRI using sensitivity encoding. *J Magn Reson Imaging*. 2008;27:239-245.
5. Schmitt F, Stehling MK, Turner R. *Echo-Planar Imaging: Theory, Technique and Applications*. Springer-Verlag; 1998.
6. Chen NK, Wyrwicz AM. Optimized distortion correction technique for echo planar imaging. *Magn Reson Med*. 2001;45:525-528.
7. Chen NK, Oshio K, Panych LP. Application of k-space energy spectrum analysis to susceptibility field mapping and distortion correction in gradient-echo EPI. *Neuroimage*. 2006;1:609-622.
8. Shrot Y, Frydman L. Spatially encoded NMR and the acquisition of 2D magnetic resonance images within a single scan. *J Magn Reson Imaging*. 2005;172:179-190.
9. Tal A, Frydman L. Spatial encoding and the single-scan acquisition of high definition MR images in inhomogeneous fields. *J Magn Reson*. 2006;182:179-194.
10. Bao Q, Liberman G, Solomon E, Frydman L. High-resolution diffusion MRI studies of development in pregnant mice visualized by novel spatiotemporal encoding schemes. *NMR Biomed*. 2020;33:e4208.
11. Schmidt R, Seginer A, Frydman L. Interleaved multishot imaging by spatiotemporal encoding: a fast, self-referenced method for high-definition diffusion and functional MRI. *Magn Reson Med*. 2016;75:1935-1948.
12. Reeder SB, Atalar E, Faranesh AZ, McVeigh ER. Referenceless interleaved echo-planar imaging. *Magn Reson Med*. 1999;41:87-94.
13. Ahn CB, Cho ZH. Analysis of the eddy-current induced artifacts and the temporal compensation in nuclear magnetic resonance imaging. *IEEE Trans Med Imaging*. 1991;10:47-52.
14. Ben-Eliezer N, Irani M, Frydman L. Super-resolved spatially encoded single-scan 2D MRI. *Magn Reson Med*. 2010;63:1594-1600.
15. Grieve SM, Blamire AM, Styles P. Elimination of Nyquist ghosting caused by read-out to phase-encode gradient cross-terms in EPI. *Magn Reson Med*. 2002;47:337-343.
16. Hu X, Le TH. Artifact reduction in EPI with phase-encoded reference scan. *Magn Reson Med*. 1996;36:166-171.
17. Xu D, King KF, Zur Y, Hinks RS. Robust 2D phase correction for echo planar imaging under a tight field-of-view. *Magn Reson Med*. 2010;64:1800-1813.
18. Zur Y. Two-dimensional phase correction method for single and multi-shot echo planar imaging. *Magn Reson Med*. 2011;66:1616-1626.
19. Nk C, Wyrwicz AM. Removal of EPI Nyquist ghost artifacts with two-dimensional phase correction. *Magn Reson Med*. 2004;51:1247-1253.
20. Seginer A, Schmidt R, Leftin A, Solomon E, Frydman L. Referenceless reconstruction of spatiotemporally encoded imaging data: principles and applications to real-time MRI. *Magn Reson Med*. 2014;72:1687-1695.
21. Chen Y, Liao Y, Yuan L, et al. Referenceless one-dimensional Nyquist ghost correction in multicoil single-shot spatiotemporally encoded MRI. *Magn Reson Imaging*. 2017;37:222-233.
22. Lee J, Han Y, Ryu JK, Park JY, Ye JC. k-Space deep learning for reference-free EPI ghost correction. *Magn Reson Med*. 2019;82:2299-2313.
23. Chen X, Zhang Y, She H, Du YP. Reference-free correction for the Nyquist ghost in echo-planar imaging using deep learning. In: *Proceedings of the IEEE International Conference on Biomedical and Bioinformatics Engineering* 2020.
24. Wang L, Wang C, Wang F, Chu YH, Yang Z, Wang H. EPI phase error correction with deep learning (PEC-DL) at 7 T. *Magn Reson Med*. 2022;88:1775-1784.
25. Ronneberger O, Fischer P, Brox T. U-net: convolutional networks for biomedical image segmentation. In: *Proceedings of the IEEE International Conference on Medical Image Computing and Computer-Assisted Intervention*, Munich, Germany 2015.
26. Korkmaz Y, Dar SUH, Yurt M, Ozbey M, Cukur T. Unsupervised MRI reconstruction via zero-shot learned adversarial transformers. *IEEE Trans Med Imaging*. 2022;41:1747-1763.
27. Shi Y, Daunhawer I, Vogt JE, Torr P, Sanyal A. How robust is unsupervised representation learning to distribution shift? In: *Proceedings of the International Conference on Learning Representations* 2022.
28. Lubis L, Cokrokusumo H, Basith R, et al. Noise reduction of three-dimensional rotational angiography (3DRA) images using residual encoder-decoder convolutional neural network. In: *Proceedings of the Physics Contribution in Medicine and Biomedical Applications* 2021.
29. Tsao J, Jiang Y. Hierarchical IDEAL: robust water-fat separation at high field by multiresolution field map estimation. In: *Proceedings of the 16th Annual Meeting of ISMRM*, Toronto, Ontario, Canada, 2008. p653.
30. Sharma SD, Hu HH, Nayak KS. Accelerated water-fat imaging using restricted subspace field map estimation and compressed sensing. *Magn Reson Med*. 2012;67:650-659.
31. Bao Q, Xie W, Otikovs M, et al. Unsupervised cycle-consistent network using restricted subspace field map for removing susceptibility artifacts in EPI. *Magn Reson Med*. 2023;90:458-472.
32. Tal A, Frydman L. Single-scan multidimensional magnetic resonance. *Prog Nucl Magn Reson Spectrosc*. 2010;57:241-292.
33. He K, Zhang X, Ren S, Sun J. Deep residual learning for image recognition. In: *Proceedings of the IEEE Conference on Computer Vision and Pattern Recognition*, Las Vegas, Nevada, USA 2016.
34. de Leeuw den Bouter ML, Ippolito G, O'Reilly TPA, Remis RF, van Gijzen MB, Webb AG. Deep learning-based single image super-resolution for low-field MR brain images. *Sci Rep*. 2022;12:6362.
35. Van Essen DC, Smith SM, Barch DM, et al. The WU-Minn human connectome project: an overview. *Neuroimage*. 2013;80:62-79.
36. Glasser MF, Sotiropoulos SN, Wilson JA, et al. The minimal preprocessing pipelines for the Human Connectome Project. *Neuroimage*. 2013;80:105-124.
37. Hennig J, Nauherth A, Friedburg H. RARE imaging: a fast imaging method for clinical MR. *Magn Reson Med*. 1986;3:823-833.
38. Wang Z, Bovik AC, Sheikh HR, Simoncelli EP. Image quality assessment: from error visibility to structural similarity. *IEEE Trans Image Process*. 2004;13:600-612.
39. Kingma DP, Jimmy B. Adam: a method for stochastic optimization. *arXiv*. 2014:1412.6980.

40. Ahn CB, Cho ZH. A new phase correction method in NMR imaging based on autocorrelation and histogram analysis. *Magn Reson Med.* 1987;6:32-36.
41. Jafari R, Spincemaille P, Zhang J, et al. Deep neural network for water/fat separation: supervised training, unsupervised training, and no training. *Magn Reson Med.* 2021;85:2263-2277.
42. Pipe JG. Spatial encoding and reconstruction in MRI with quadratic phase profiles. *Magn Reson Med.* 1995;33:24-33.
43. Chen Y, Li J, Qu X, et al. Partial Fourier transform reconstruction for single-shot MRI with linear frequency-swept excitation. *Magn Reson Med.* 2013;69:1326-1336.
44. Liu S, Thung K-H, Qu L, Lin W, Shen D, Yap P-T. Learning MRI artefact removal with unpaired data. *Nat Machine Intel.* 2021;3:60-67.
45. Ahmad W, Ali H, Shah Z, Azmat S. A new generative adversarial network for medical images super resolution. *Sci Rep.* 2022;12:9533.
46. Zhang K, Hu H, Philbrick K, et al. SOUP-GAN: super-resolution MRI using generative adversarial networks. *Tomography.* 2022;8:905-919.
47. Liberman G, Solomon E, Lustig M, Frydman L. Multiple-coil k-space interpolation enhances resolution in single-shot spatiotemporal MRI. *Magn Reson Med.* 2018;79:796-805.
48. Chen NK, Guidon A, Chang HC, Song AW. A robust multi-shot scan strategy for high-resolution diffusion weighted MRI enabled by multiplexed sensitivity-encoding (MUSE). *Neuroimage.* 2013;72:41-47.

SUPPORTING INFORMATION

Additional supporting information may be found in the online version of the article at the publisher's website.

Figure S1. Details of the conventional Nyquist-ghost correction method of single-shot spatiotemporal encoding (SPEN). First, separate the even and odd rows of the original phase-distorted SPEN data, and perform Fourier transform (FT) along the readout (RO) direction to obtain low-resolution odd echo image S_{odd} and even echo image S_{even} . Second, perform superresolution (SR) reconstruction along the phase-encoding (PE) dimension to obtain high-resolution odd echo image $\hat{\rho}_{\text{odd}}$ and even echo image $\hat{\rho}_{\text{even}}$. Then, perform the quadratic polynomial fitting on $\hat{\rho}_{\text{odd}}$ and $\hat{\rho}_{\text{even}}$ to unwrap the phase difference map θ_{dif} , which is used to correct the phase of S_{even} to keep consistent with the phase of S_{odd} . Next, recombine the phase-corrected, low-resolution, even echo image $S_{\text{even}}^{\text{cor}}$ with S_{odd} and obtain a full low-resolution, phase-corrected SPEN image S^{cor} . Finally, perform SR reconstruction along the PE dimension to obtain a high-resolution ghost-corrected SPEN image $\hat{\rho}^{\text{cor}}$.

Figure S2. The structure of supervised and unsupervised method. (A) The Supervised-1 method directly inputs the image into the network, then outputs the image. First, the uncorrected, low-resolution image is transformed into an uncorrected, high-resolution image through superresolution, and then the uncorrected,

high-resolution image is sent to the Dense-net or U-net network to obtain the corrected image. Next, the loss between the corrected image and the true value image is calculated. (B) The Supervised-2 method inputs the odd and even echo images into the Dense-net or U-net to obtain a phase map. The phase map is used to correct the even echo image and then combine with the odd echo image to obtain a corrected low-resolution image. Finally, the corrected high-resolution image is obtained through superresolution, and the loss is calculated using this image and the true value image. (C) The proposed unsupervised method.

Figure S3. Details of the production process of simulated data. After setting the parameters of the single-shot spatiotemporal encoding (SPEN) pulse sequence used in the simulation, the T_1 -weighted (T1w) anatomical images of the human brain were sampled using the SPEN sequence, and Fourier transform (FT) along the readout (RO) direction was performed to obtain low-resolution SPEN images S . Then, the odd and even echoes of S were separated, and random linear/nonlinear phases were applied to the even echo images S_{even} . Phase-distorted even echo images $S_{\text{even}}^{\text{dis}}$ and the original odd echo images S_{odd} were used as the simulated data for RERSM-net. Finally, $S_{\text{even}}^{\text{dis}}$ and S_{odd} were recombined to obtain full phase-distorted SPEN images S^{dis} as the simulated data for the conventional method. Because Human Connectome Project (HCP) T1w images contained only magnitude and no phase information, to obtain an actual k-space, a phase for T1w images was generated. This was performed by creating a 3×3 matrix of random numbers. This 3×3 matrix was zero-padded to the corresponding T1w image size and Fourier-transformed. Because only elements at the center of this matrix corresponding to an area of 3×3 were distinct from zero, the Fourier-transformed matrix contained only low-frequency information equivalent to a smooth phase. The final image used as an input to simulation was obtained by multiplying the T1w image with a complex exponential of the generated phase map. To obtain image S , the SPEN pulse sequence depicted in Figure 1A was simulated with the corresponding acquisition and encoding parameters: FOV = $4 \times 4 \text{ cm}^2$, sampling matrix = 256×256 (readout [RO] \times phase encode [PE]), effective TE = 36 ms, TR = 4 s, R value of chirp pulse = 400, and pulse length = 18 ms. A total of 32 spins per voxel were used to avoid discontinuities, and the simulations were performed in *MATLAB* using the Spintool package (Tal 2020; Visual Display Interface [VDI] computer software; retrieved from <http://www.vdisoftware.net>).

Figure S4. Detailed structure of U-net used for comparative experiment.

Figure S5. Comparison of the proposed Residual Encoder and Restricted Subspace Mapping (RERSM-net) and

U-net. (A) The first row from left to right shows the uncorrected ghost image, ground-truth image, and ghost-corrected images by U-net and the proposed RERSM-net, respectively. The second row shows the zoomed region of the first row's images. The third row shows the absolute error maps. The fourth row shows the phase difference maps. (B) Quantitative results of peak SNR (PSNR) and structural similarity measurement (SSIM) for various comparison methods.

Figure S6. Comparison between the proposed Residual Encoder and Restricted Subspace Mapping network (RERSM-net) and the ablation experiment with residual structure removed by the network (A) shows the ground-truth image and uncorrected ghost image; the corrected images of the RERSM-net without residual structure and the complete RERSM-net are presented in the first row from left to right. The second row shows

the zoomed area of the first-row image. The third line displays the absolute error map (differences between the Nyquist ghost-corrected image and ground-truth image). The fourth line shows the phase difference plot. (B) Quantitative results of peak SNR (PSNR) and structural similarity measurement (SSIM) for various comparison methods.

Table S1. Pulse sequence parameters.

Table S2. Details of the used U-net in this study.

How to cite this article: Bao Q, Liu X, Xu J, et al. Unsupervised deep learning model for correcting Nyquist ghosts of single-shot spatiotemporal encoding. *Magn Reson Med*. 2024;91:1368-1383. doi: 10.1002/mrm.29925